Thermal Runaway in Lithium-Ion Batteries: Modeling, Experimental Validation, and Material Effects on Propagation

Sevgi AYDIN[*1] |Kadri Süleyman YİĞİT[1] |İsmail Hakkı SAVCI[2]

[1]Kocaeli University, Department of Mechanical Engineering, 41380, Kocaeli, Türkiye.
[2]Ford Otosan, 34885, Istanbul, Türkiye.

Corresponding Author
Sevgi Aydın
E-mail: sevgi.57.aydin@gmail.com
RORID[1]: https://ror.org/0411seq30 RORID[2]: https://ror.org/04h48jk55

Cite As

Aydın S., Yiğit KS., Savcı İH. Thermal runaway in lithium-ion batteries: modeling, experimental validation, and material effects on propagation. Hittite J Sci Eng. 2025;12(4):209-221.

Peer Review: Evaluated by independent reviewers working in at least two different institutions appointed by the field editor.
Ethical Statement: Not available.
Plagiarism Checks: Yes - iThenticate
Conflict of Interest: Authors approve that to the best of their knowledge, there is not any conflict of interest or common interest with an institution/ organization or a person that may affect the review process of the paper.

CRediT AUTHOR STATEMENT
Sevgi AYDIN: Conceptualization, Methodology, Software, Validation, Data curation, Visualization, Investigation, Writing- original draft. **Kadri Süleyman YİĞİT:** Validation, Supervision, Writing- review and editing. **İsmail Hakkı SAVCI:** Conceptualization, Validation, Supervision, Writing- review and editing.

Thermal Runaway in Lithium-Ion Batteries: Modeling, Experimental Validation, and Material Effects on Propagation

Sevgi AYDIN[*1] | Kadri Süleyman YİĞİT[1] | İsmail Hakkı SAVCI[2]

[1]Kocaeli University, Department of Mechanical Engineering, 41380, Kocaeli, Türkiye.
[2]Ford Otosan, 34885, Istanbul, Türkiye.

Abstract

The thermal safety of lithium-ion batteries (LIBs) is a crucial challenge for electric vehicles and stationary energy storage systems, as excessive heat generation may cause accelerated aging, capacity loss, or catastrophic thermal runaway (TR). This study develops and validates a coupled electrochemical–thermal model to investigate the heat generation, temperature response, and TR behavior of cylindrical 18650-type LIBs. Experimental discharge tests (1C and 2C) were performed on a 1S14P battery module, and the results were compared with numerical simulations in STAR-CCM+ and an Arrhenius-based TR model implemented in MATLAB Simulink. The model accurately captured the onset of exothermic reactions, with a maximum deviation of ~5% from experimental data. Parametric analyses revealed that higher ambient convection coefficients delay TR initiation and reduce its severity, highlighting the importance of forced-air cooling in thermal management systems. Furthermore, the effect of different enclosure materials on TR propagation was investigated. While ceramic fiber and aerogel provided the most effective thermal insulation, polystyrene demonstrated the best overall balance between heat dissipation under normal operation and insulation during TR events. The findings confirm that material selection and thermal management design play a decisive role in preventing TR propagation and ensuring battery safety. This work contributes practical guidelines for the safe and efficient design of next-generation battery systems.

Keywords: Lithium-ion battery, Thermal runaway, Battery safety, Battery thermal management, Battery cooling

INTRODUCTION

With the rapid advancement of science and technology, global energy demand continues to rise, raising concerns over the depletion of fossil fuel resources. As a result, sustainable energy systems are gaining prominence, and fossil-fuel-based systems are increasingly being replaced by electricity-driven technologies [1]. Among these, lithium-ion batteries (LIBs) have emerged as the dominant energy storage solution due to their high energy density, long cycle life, and low self-discharge rates. They are now widely used in portable electronics, electric vehicles (EVs), and large-scale stationary storage systems. [2, 3]. Despite these advantages, LIB safety remains a critical concern. Excessive heat generation during charge–discharge cycles can accelerate capacity fading, reduce service life, and under severe conditions, trigger thermal runaway (TR)—a chain reaction of exothermic processes that may lead to fire or explosion. Several high-profile accidents, including EV recalls and large-scale energy storage fires, have drawn public and industrial attention to the urgent need for safer battery technologies. Table 1 lists examples of lithium-ion battery incidents reported in the media.

Excessive heat generation during charging and discharging can accelerate capacity fading, shorten lifespan, and, under severe conditions, trigger thermal runaway (TR), potentially leading to fire or explosion. In response to these safety concerns, regulations and standards have been introduced to ensure the safe inspection, usage, and shipment of battery systems [4-9].

The operating temperature of battery systems is a critical factor for achieving optimal lifespan, power output, and operational safety. For lithium-ion batteries, the acceptable operating temperature range is between -20°C and 60°C, with the optimal range being 15°C to 35°C [10-13]. The primary sources of heat in LIBs include electrochemical reaction heat, ohmic resistance heat, and side reaction heat. If the heat generation rate exceeds the heat dissipation capacity, the cell temperature rises uncontrollably, creating a feedback loop that increases reaction rates and further accelerates heating. Such phenomena underscore the importance of effective thermal management systems (TMS) for preventing TR and ensuring safe battery operation. To ensure safe operation, the thermal and electrical conditions of battery cells must be controlled and isolated from each other [10-13].

Table 1 Lithium-ion battery power system accidents reported in the press.

Year	Accident
2010	The Boeing 747 cargo plane crashed on a deserted island due to a fire caused by the batteries. Two crew members died. Following this incident, airline companies began to make decisions banning the shipment of batteries [6].
2016	The SAMSUNG company recalled its Note 7 series phones from the market due to a faulty battery casing design that caused them to overheat and catch fire [7].
2020	Hyundai Motor recalled the Kona model vehicles worldwide due to faulty batteries causing them to catch fire in various locations around the world [8].
2021	In Austria, at the Victorian Big Battery facility, a Tesla Megapack BESS unit caught fire. There were no casualties in this incident, but a significant amount of toxic gas was released into the environment [8].
2022	In the United States, the S-Trust ship caught fire due to a thermal runaway of its. Many systems onboard the ship were irreparably damaged. The incident caused damage amounting to 3 million dollars to the ship and the terminal [9].
2018-2023	Electric vehicles catching fire due to thermal runaway caused by battery damage following collisions have drawn press and public attention to electric vehicles [8].

Thermal, electrical, or mechanical abuse of lithium-ion batteries can result in dangerous scenarios such as uncontrollable heating, high temperatures, explosions, or

fires—a phenomenon known as thermal runaway [13-16]. When a battery's temperature exceeds 90°C, the solid electrolyte interface (SEI) on the cathode begins to decompose. At 100-120°C, the SEI melts completely, leading to contact between the anode and cathode, which causes short circuits and accelerates exothermic reactions. This process increases cell temperature rapidly, releasing flammable gases such as O_2, CO_2, and H_2. At 200°C, these gases ignite, resulting in a fire. The exothermic reactions persist until the energy within the cell is depleted, after which the temperature gradually decreases [10, 13, 15, 17].

Hatchard et al. [18] conducted the first experimental and numerical investigations on thermal runaway (TR), examining the runaway behavior under different oven temperatures. Parhizi et al. [19] developed numerical schemes to accelerate the solution of differential equations governing TR models and reported results consistent with commercial software. Ostanek et al. [20] incorporated mass and energy conservation into TR models and analyzed gas generation and ventilation processes. Kim et al. (21) performed 3D Fluent simulations considering reaction chemistry, cell geometry, and material effects, and emphasized that cell size strongly influences thermal behavior in oven test simulations. Peng et al. [22] reported that positive electrode reactions dominate heat release during TR, while higher oven heat transfer coefficients increase the critical onset temperature. Özdemir et al. [23] induced TR using heater films under various charge conditions and developed an Arrhenius-based model predicting initiation and peak temperature with ~10% error. Similarly, Shen et al. [24] estimated heat generation as a function of capacity, voltage, and volume. Chen et al. [25] simulated the thermal runaway process by defining heat generation for 10 seconds instead of creating a traditional thermal runaway model.

The propagation of TR from a failed cell to neighboring cells is a critical safety issue [10, 11, 27]. Citarella et al. [27] showed that minimizing inter-cell heat transfer in module design improves safety. Li et al. [28] simulated TR propagation in an air-cooled pack, while Zhong et al. [29] demonstrated that inter-cell gaps have limited effect, with 4 mm being sufficient to mitigate thermal shock. Silva et al. [30] and Lee et al. [31] highlighted that ceramic fiber boards are highly effective, slowing TR heat transfer by up to 30 times. Quan et al. [32] emphasized the importance of insulation material selection, and Li et al. [33] showed that aluminum frames can absorb heat and prevent TR spread. Other studies explored alternative thermal barrier materials; Yuan et al. [34] reported that graphite sheets suppress TR due to low thermal conductivity, while Zhao et al. [35] found graphite heat shields effective for safety during storage and transportation. Nambisam et al. [36] evaluated commercial thermal barrier materials such as mica, fiberglass, and ceramics, and found them suitable when thickness and design constraints are considered.

Beyond modeling and passive barrier strategies, recent studies have focused on hybrid suppression approaches combining multiple thermal management mechanisms. Hybrid prevention and suppression strategies typically combine multiple thermal management mechanisms, such as

PCM with insulation, PCM with liquid cooling, or chemical and thermal reactions. Tianqi Yang et al. [37] combined SAT-EG-based composite phase change material with liquid cooling in prismatic battery modules, delaying TR propagation by more than six times and fully preventing TR when SAT-EG thickness exceeded 12 mm. Liu et al. [38] numerically modeled a 12-cell prismatic battery pack using PPCM combined with insulation layers and immersion cooling with fluorinated liquids; the 3.6 mm PPCM and 1 mm insulation combination extended the TR trigger time of the second cell to 798 s, while the average temperature of Cells around 34 °C, fully preventing propagation. Weigao Ji et al. [39] integrated nano-ceramic fiber-based PCM with liquid-cooled plates in high-specific-energy pouch cells, implementing a three-level TR protection strategy consisting of early heat absorption, intermediate heat conduction, and delayed heat insulation; this approach kept the second cell's maximum surface temperature below 100 °C after TR initiation and successfully prevented TR propagation. Collectively, these studies demonstrate that hybrid strategies combining PCM and liquid cooling are effective in delaying or preventing TR propagation in batteries. Choi et al. [40] experimentally investigated early detection and suppression strategies of thermal runaway in large-format lithium-ion batteries, demonstrating that CO_2 injection and rapid water intervention effectively prevent propagation.

In our study, TR processes of LIBs were comprehensively examined using a numerical model based on Arrhenius equations. The influence of ambient temperature and convection coefficient on TR was analyzed, and the effect of different module housing materials on TR propagation was evaluated through numerical simulations. The accuracy of the modeling approach was validated against discharge test data.
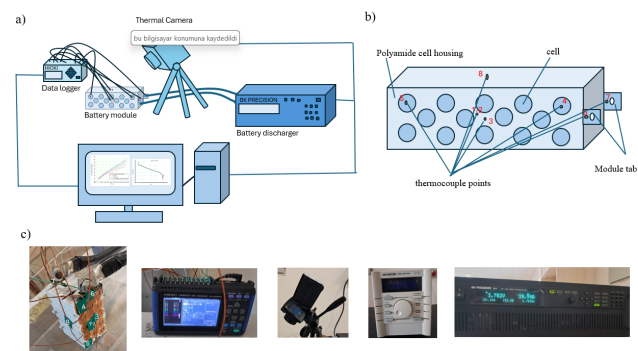

Figure 1 Experimental setup: (a) schematic of the test configuration, (b) schematic of the module layout and thermocouple positions, (c) battery module and test devices (data logger, thermal camera, power supply, and load).

MATERIAL AND METHODS

Experimental method

In this study, a 40-ampere battery module was developed with a 1S14P configuration using cylindrical 18650 cells. Each cell has a nominal voltage of 3.65 V and an energy capacity of 2800 mAh. The key dimensional and thermophysical characteristics of the battery cells are summarized in Table 2. The cells were securely housed in polyamide-based enclosures to ensure structural integrity. The cells were securely housed in polyamide-based enclosures to ensure structural integrity.

The thermophysical properties of the tested materials, including the polyamide enclosure, are presented in Table 3.

Table 2 Dimensional and thermophysical characteristics of the battery cells [40].

	Value	Unit
Dimensional properties;		
Cell diameter	18+0,10/-0,20	mm
Cell length	65±0,2	mm
Weight	44,5±0,7	g
Battery chemistry;		
Anode	Graphite based coating on copper foil	
Cathode	NiMnCo(NMC) based coaing on aluminum foil	
Thermo-phisical specification;		
Density	2746	kg/m³
Specific heat	1065,71	j/kg.K
Thermal conductivity	33	W/m.K

Charging and Discharging Protocol;
The battery module was charged with a constant current of 18 A until reaching a maximum voltage of 4.2 V. Discharge tests were conducted at 1C and 2C rates, with the discharge cut-off voltage set at 2.4 V. Before each charge–discharge cycle, the module was allowed to cool to room temperature to ensure repeatability. Charging was carried out using a GOODWILL INSTEK PSH-2018A DC power supply, and discharging was performed with a BK Precision 8614 DC electronic load under natural convection conditions.

Table 3 Module housing material properties [41-44, 46].

Material	Density [kg/m³]	Specific Heat [J/kg.K]
Polyamide	1635	700
Aerogel	500	1000
Flame-resistant graphite composite	1700	800
Epoxy-filled carbon fiber	1500	700
Rubber	1100	1500
Mica	2800	880
Polypropylene	900	1920
Polystyrene	1040	1300
PVC	1300	100
Ceramic	800	2500
Ceramic fiber	100	1000
Teflon	2150	1000

Thermal Data Collection;
Temperature data were recorded in real time using a Hioki LR8431-20 memory logger equipped with thermocouples,

while thermal imaging was performed with a Testo 885 thermal camera. The experimental setup and the equipment used are presented in Figure 1, which shows the battery module consisting of 14 cells placed inside the polyamide-based enclosure, along with the images of the test devices and the schematic representation of the setup.
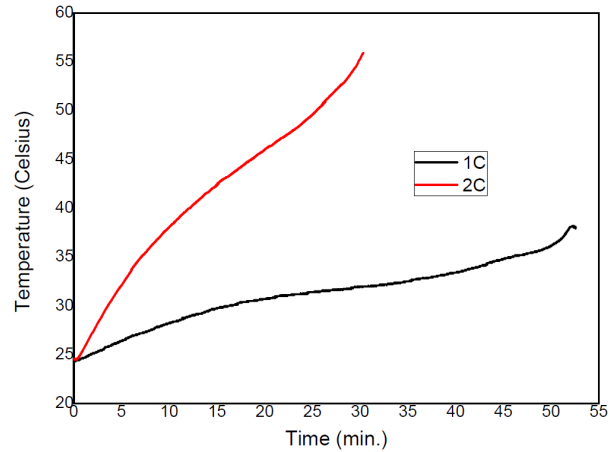

Figure 2 Time-dependent temperature profiles of the lithium-ion cell at 1C and 2C discharge rates [40].

Table 4 Parameters of the Arrhenius thermal runaway model [18, 30].

Frequency factor;		
A_{sei}	1.667×10^{15}	()
A_{AnE}	2.5×10^{13}	
A_{CaE}	6.667×10^{13}	
A_E	5.14×10^{25}	
Activation energy;		
E_{sei}	1.3508×10^{5}	(J/mol)
E_{AnE}	1.3508×10^{5}	
E_{CaE}	1.396×10^{5}	
E_E	2.74×10^{5}	
Specific heat;		
E_{sei}	2.57×10^{5}	(J/kg)
E_{AnE}	1.714×10^{6}	
E_{CaE}	3.14×10^{5}	
E_E	1.55×10^{5}	
Reaction order;		
m_{sei}	1	-
m_{AnE}	1	
m_{CaE}	1	
m_E	1	
Cell mass content;		
W_c	1.39×10^{3}	kg/m³
W_p	1.3×10^{3}	
W_E	5×10^{2}	
Initial Condition;		
$c_{sei,0}$	0.15	-
$c_{AnE,0}$	0.75	
$c_{CaE,0}$	0.04	
$c_{E,0}$	1	
T_{sei}	0.033	

To determine the heat generation during discharge, thermocouples were placed at the top, middle, and bottom of the cell surface at room temperature. The cell was insulated to minimize external heat loss and discharged at 1C and 2C rates. The resulting temperature data are presented in Figure 2.

Numerical Model and Thermal Runaway Processes

The battery energy balance is calculated according to Eq. (1), where the battery temperature varies as a function of time:

$$\rho \cdot c_p \cdot \frac{\delta T}{\delta t} = \nabla \cdot k \cdot \nabla T + q_{gt} + q_{tr}(t) \tag{1}$$

Here, ρ is the cell density (kg/m³), cp the specific heat capacity (J/K.kg), T the temperature (K), k the thermal conductivity coefficient (W/m.K). q_g and q_t represent volumetric heat generation inside the cell and heat transfer to the environment (W/m³) respectively. q_g caused by TR are defined as:

$$q_g = q_{sei} + q_{AnE} + q_{CaE} + q_E \tag{2}$$

The first exothermic reaction within the cell begins with the decomposition of the solid electrolyte interphase (SEI) as the cell temperature exceeds 90°C [17, 30]. The Arrhenius TR mathematical model heat generation equations for SEI decomposition are given in Eq. 3-5. SEI decomposition mathematical model block diagrams are given in Figure 3. The Arrhenius thermal runaway mathematical model parameters are given in Table 4-5.
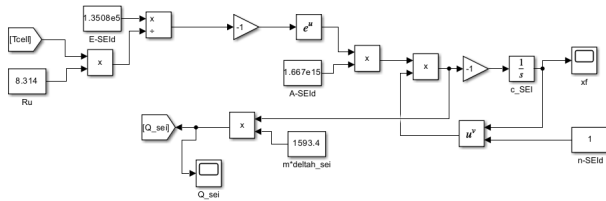
Figure 3 Arrhenius-based mathematical model Simulink block diagram of thermal runaway SEI decomposition.

$$q_{sei} = H_{sei} \cdot W_c \cdot R_{sei} \tag{3}$$

$$R_{sei}\left(T, c_{sei}\right) = A_{sei} \cdot exp\left[-\frac{E_{a,sei}}{R \cdot T}\right] \cdot c_{sei}^{m_{sei}} \tag{4}$$

$$\frac{dc_{sei}}{dt} = -R_{sei} \tag{5}$$

As the SEI layer decomposes, the anode electrode becomes vulnerable to reacting with the electrolyte liquid. When the battery temperature exceeds 120°C, exothermic reactions begin to occur between the organic solvents in the electrolyte and the lithium ions in the anode [18, 45]. The Arrhenius TR mathematical model anode heat generation equations are provided in Eq. 6-8 and Block diagram of it are given in Figure 4.
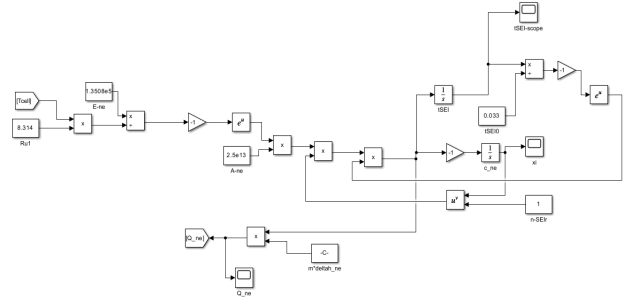
Figure 4 Arrhenius-based mathematical model Simulink block diagram of thermal runaway anode reactions.

$$q_{AnE} = H_{AnE} \cdot W_c \cdot R_{AnE} \tag{6}$$

$$R_{AnE}\left(T, c_{AnE}, t_{sei}\right) = A_{AnE} \cdot exp\left[-\frac{T_{sei}}{T_{sei,ref}}\right] \cdot c_{AnE}^{m_{AnE}} \cdot exp\left[-\frac{E_{a,AnE}}{R \cdot T}\right] \tag{7}$$

$$\frac{dc_{AnE}}{dt} = -R_{AnE}, \frac{d\mathcal{T}_{AnE}}{dt} = -R_{AnE} \tag{8}$$

As the temperature rises, reactions between the cathode and electrolyte are triggered. The Arrhenius TR mathematical model equations for exothermic reactions between the cathode electrode and the electrolyte liquid are given in Eq. (9–11) and illustrated in Figure 5.
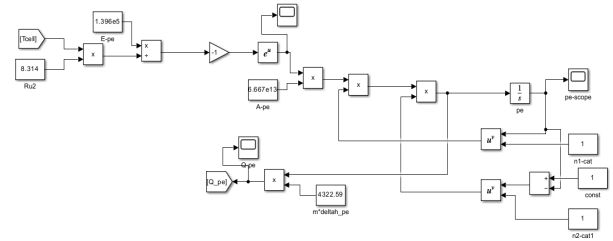
Figure 5 Arrhenius-based mathematical model Simulink block diagram of thermal runaway cathode reactions.

Table 5 Additional parameters of the Arrhenius thermal runaway model [18, 30].

Cell Volume (V_{cell})	4.665 x10⁻⁵	m³
Reaction Percentage per Cell Volume ($V_{reaction}$)	63.6	(%)
Convection Coefficient (h)	7.17	W/m².K
Cell Surface Emissivity (ε)	0.8	-
Cell Surface Area (A_{cell})	4.37 x10⁻³	m³
Specific Heat Capacity of the Cell (c_p)	1280	J/kg.K
Cell density (ρ)	2939	kg/ m³

$$q_{CaE} = H_{CaE} \cdot W_p \cdot R_{CaE} \tag{9}$$

$$R_{CaE}\left(T, \alpha\right) = A_{CaE} \cdot \alpha^{m_{CaE}} \cdot \left(1 - \alpha\right)^{m_{CaE}} \cdot exp\left[-\frac{E_{a,CaE}}{R \cdot T}\right] \tag{10}$$

$$\frac{d\alpha}{dt} = R_{CaE} \tag{11}$$

Electrolyte decomposition begins when the battery temperature reaches 150°C, and the amount of energy release

increases further. The Arrhenius electrolyte decomposition TR mathematical model equations is given Eq. 12-14 and Figure 6.

$$q_E = H_E \cdot W_E \cdot R_E \tag{12}$$

$$R_E\left(T, c_E\right) = A_E \cdot exp\left[-\frac{E_{a,E}}{R \cdot T}\right] \cdot c_E{}^{m_E} \tag{13}$$
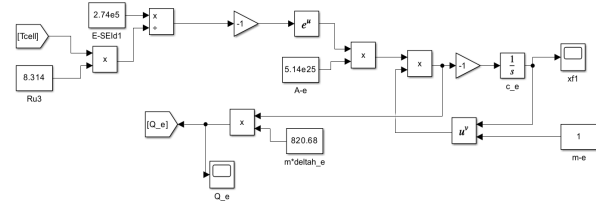
$$\frac{dc_E}{dt} = -R_E \tag{14}$$

Figure 6 Arrhenius-based mathematical model Simulink block diagram of thermal runaway electrolyte decomposition reactions.

Since the cell is exposed to air, convection and radiation dominate heat transfer to the surroundings, were expressed by Eq. (15–17) and Figure 7. ε is the surface emissivity, σ the Stefan-Boltzmann constant (W/m^2.K^4), $T_{surface}$ the cell surface temperature (K), T_{amb} the ambient temperature (K), A_{cell} the cell surface area (m^2) and h the convective heat transfer coefficient (W/ m^2.K).

$$Q_{transfer}(t) = Q_{radiation,surface}(t) + Q_{convection}(t) \tag{15}$$

$$Q_{radiation,surface} = \varepsilon \cdot \sigma \cdot A_{cell} \cdot \left(T_{surface}{}^4(t) + T_{amb}{}^4(t)\right) \tag{16}$$

$$Q_{convection,surface} = h \cdot A_{cell} \cdot \left(T_{surface}(t) + T_{amb}(t)\right) \tag{17}$$
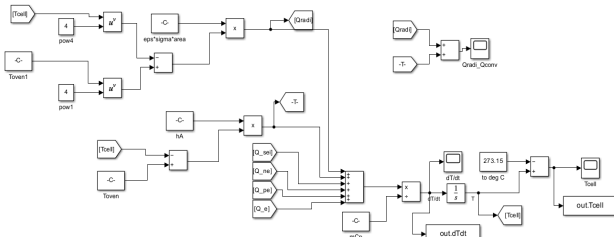
Figure 7 Block diagram of the overall thermal runaway energy balance.

A comparative analysis of thermal runaway behavior at 155 °C oven temperature is shown in Figure 8, including Silva et al. [30], Hatchard et al. [18], and our simulation results. Our findings closely match Hatchard's numerical model, with an average deviation of only ~3%. The earlier onset of thermal runaway in Silva's study stems from its higher initial temperature.

As illustrated, internal heat generation is initially lower than external heating. Once temperature rises, decomposition of the SEI layer initiates, followed by electrolyte breakdown and separator melting. This leads to internal short circuiting, rapid temperature escalation, increased gas production, and eventually venting when the internal pressure surpasses critical thresholds. In later stages, flame ejections may occur.
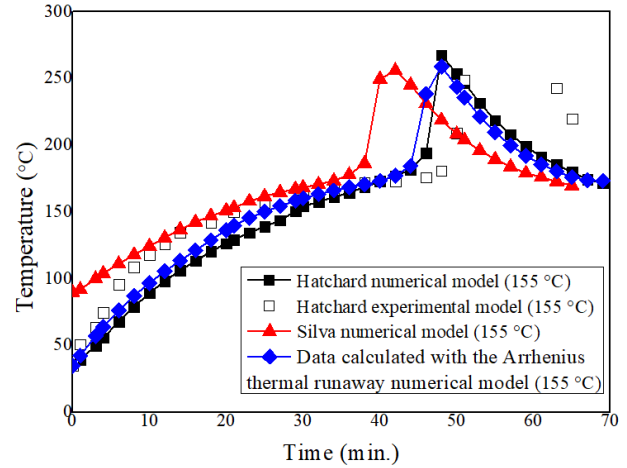
Figure 8 Time-dependent cell temperature variation at 155°C oven temperature.

Deviations between simulation and experimental results mainly arise from phenomena not directly modeled, such as gas combustion and electrode material expulsion under pressure. To more accurately capture real thermal behavior, these effects should be incorporated into the Arrhenius framework. Nevertheless, the present numerical model provides reliable insights into the progression of thermal runaway, even if it cannot exactly reproduce maximum experimental temperatures.

Simulation Model

The lithium-ion battery module considered in this study consists of 14 cylindrical 18650-type cells connected in parallel, as shown in Figure 9. Discharge tests were conducted under natural convection at 1C and 2C rates, and the results were compared with STAR-CCM$^+$ simulations to validate the numerical model. The influence of cell housing materials on the thermal performance of the module was also evaluated.

In the simulations, the cells were assumed to have constant and homogeneous thermophysical properties (specific heat, density, and thermal conductivity). Heat generation was modeled as constant and dependent on the discharge rate. The governing conservation equations of mass, momentum, and energy were applied, as given below:

Mass and momentum transport equation:

$$\frac{\partial \rho}{\partial t} + \nabla\left[\rho(\bar{v} - v_g)\right] = 0 \tag{18}$$

$$\frac{\partial}{\partial t}\left(\rho\bar{v}\right) + \nabla\left[\rho\left(\bar{v}\left(\bar{v} - v_g\right)\right)\right] = -\nabla \cdot \bar{p}I + \nabla\left(\dot{T} + \dot{T}_t\right) + f_b \tag{19}$$

where ρ is the density, $\bar{v}$ and $\bar{p}$ are the mean velocity and pressure respectively, is the reference frame velocity relative to the laboratory frame, I is the identity tensor. $\dot{T}$ is the viscous stress tensor, f_b is the resultant of the body forces.

Energy Equations;

$$\frac{\partial}{\partial t} \int_V \rho CpTdV + \oint_A \rho Cpv_s \cdot da = \oint_A k\nabla T \cdot da + \int_V S_u dV \tag{20}$$

where E is the total energy, H is the total enthalpy, k is thermal conductivity factor od material, S_u is contributes energy source terms, C_p is the specific heat, T is the temperature, $\oint_A \dot{T} \cdot vda$ is viscous dissipation.
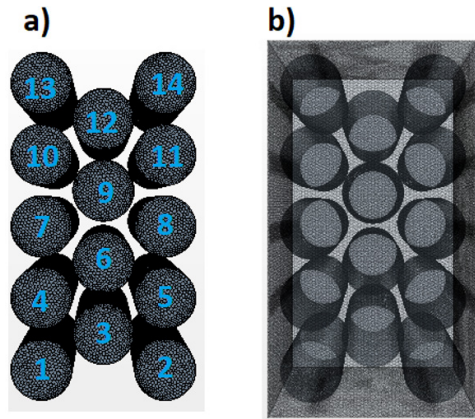

Figure 9 CAD image of the battery module a) battery cells and cell diagrams, b) battery module.

Table 5 Maximum module temperatures and percentage errors for 1C and 2C discharge rates.

	Natural convection	
	1C	**2C**
Analysis	52.3 °C	38.7 °C
Test	55.4 °C	39.9 °C
Percentage error	%5,6	%3

Mesh independence was tested to ensure accuracy of the model. Figure 10 shows the mesh validation analysis for natural convection cooling at 2C discharge. Under forced air cooling at 2C, the optimal mesh size was found to range between 130,573 and 171,233 elements. Within this range, simulation results were compared with experimental data, with a maximum percentage error of 5.6% (Table 5).
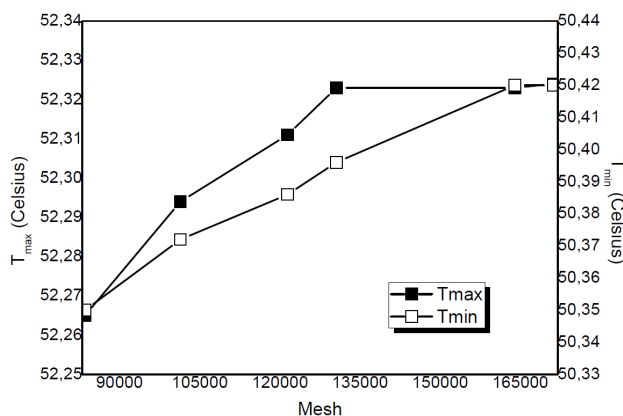

Figure 10 Mesh validation analysis under natural convection at 2C discharge rate.

After the discharge analysis, thermal runaway simulations were conducted. A fully charged battery in sleep mode was

subjected to forced runaway by heating the sixth cell with a 20 W heat source. Figure 11 presents the time-dependent temperature profile of the cell under thermal abuse. Notable differences were observed between the numerical predictions and experimental TR temperature limits; therefore, experimental temperature data were used as input for the runaway simulations.

The study also investigated the impact of thermally insulating housing materials on the thermal runaway process. Materials evaluated included ceramic, ceramic fiber, polyamide, polypropylene, flame-resistant graphite composite, epoxy-filled carbon fiber, mica, rubber, Teflon, and PVC. The thermal analysis excluded TR propagation to other cells but assessed the risk of spreading within the module. The three-dimensional numerical analysis assumed homogeneous heat generation throughout the battery volume. However, thermal effects from temperature increases in neighboring cells due to heat transfer were not considered.
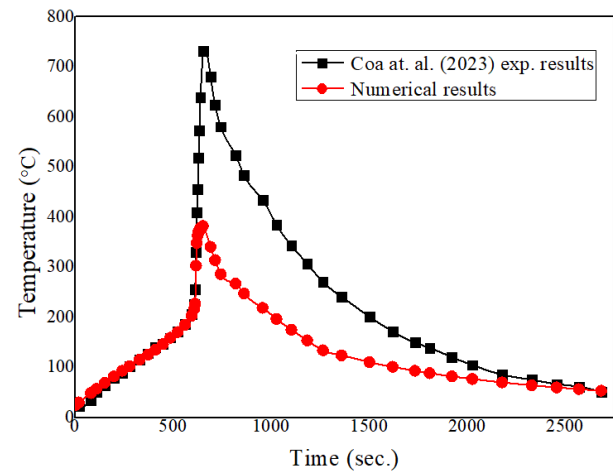

Figure 11 Temperature evolution of a battery under 20 W thermal abuse [45]

Finally, the thermal runaway process was modeled in MATLAB Simulink based on the Arrhenius equations described in Section 2.2.

RESULTS AND DISCUSSION

The severity of thermal stress affects the temperature increase and the intensity of the thermal runaway process in the battery. The numerical model results of thermal runaway due to the temperature exposure of lithium-ion batteries are presented in Figure 12. The results obtained regarding the temperature increase and thermal runaway process in the battery based on the degree of thermal stress are as follows;

• 145°C Oven Test: In the numerical analysis, the battery steadily heated up to a maximum of 150°C for the first 30 minutes. Reactions between the anode, which became vulnerable due to solid electrolyte decomposition, and organic solvents in the electrolyte, along with cathode-electrolyte reactions triggered by the rising temperature, caused the battery to heat up to 150°C. However, the considered heat dissipation conditions allowed the generated heat to be released into the

oven, preventing the battery from reaching a temperature that would trigger electrolyte decomposition. As a result, the battery gradually cooled down to the oven temperature of 145°C.

• 150°C Oven Test: The battery temperature showed a steady increase during the first 30 minutes, reaching 160°C. It remained at this temperature for approximately 40 minutes and then increased further to 220°C at the 70th minute.

• 155°C Oven Test: Numerical analyses indicate that the battery temperature exhibited a steady increase for the first 40 minutes, after which it suddenly rose to 259°C. At this temperature, the heat dissipation conditions were insufficient to release the generated heat into the oven, triggering electrolyte decomposition. Consequently, a sudden temperature rise was observed in the battery.

• 155°C and Higher Oven Tests: Similarly, at these temperature levels, the battery temperature initially showed a steady increase, but as electrolyte decomposition began, the temperature rose sharply. This sudden temperature increase due to thermal runaway led to gas accumulation and pressure buildup inside the cell. This situation increases the risk of the cell catching fire or exploding and raises the potential for thermal runaway propagation throughout the battery pack.

As the severity of thermal stress increases, the thermal runaway process starts earlier. For example, at 155°C, thermal runaway occurs around the 41st minute, whereas, in a cell exposed to 185°C, this duration decreases to as little as 20 minutes. This phenomenon is driven by three main factors:

1. Increased oven temperature raises the convective heat transfer rate from air to cell, triggering runaway earlier.

2. Higher temperatures increase the temperature gradient between the battery and surroundings, accelerating heat transfer.

3. Maximum surface temperature and temperature rise rate increase at higher oven temperatures, intensifying the thermal runaway process.

At oven temperatures above 150°C, thermal runaway occurs more aggressively. The primary reason for this is that electrolyte reactions begin above 150°C. While no electrolyte reactions occur at temperatures below 150°C, highly energetic reactions take place at higher temperatures, leading to sudden temperature spikes.

The critical temperature at which electrolyte reactions start varies depending on the battery type. The numerical model we used is based on the study by Hatchard et al. [18], which focuses on lithium cobalt oxide ($LiCoO_2$) batteries. For this battery type, the electrolyte decomposition threshold is determined to be 150°C. According to the study by Chen and Richardson [47], the required temperature for electrolyte decomposition in lithium iron phosphate ($LiFePO_4$) batteries is 250°C. The safety of a battery pack is directly related to the type of battery used.
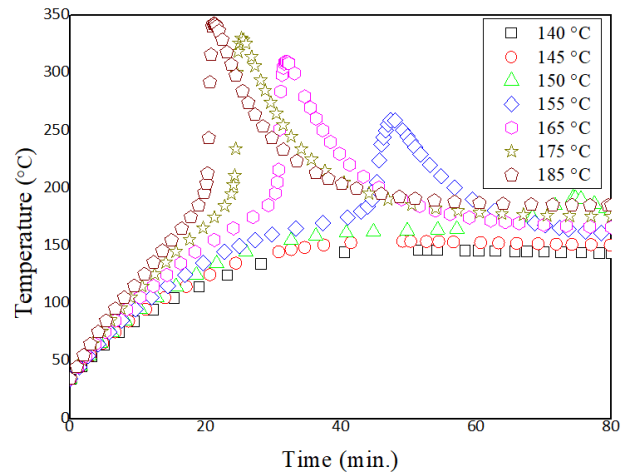

Figure 12 Numerical results of the time-dependent variation of battery temperature under different exposure temperatures (h:7,14 W/ m2K).

The effects of the convective heat transfer coefficient on the temperature response have been evaluated, and in Figure 13 the temperature–time graph of the thermal runaway process in a thermal abuse environment is presented as a function of the convective heat transfer coefficient. As the heat transfer coefficient increases, the time that the battery must remain in a high-temperature environment trigger the thermal runaway process decreases. An increase in the heat transfer coefficient enhances the efficiency of heat transfer, enabling the battery to reach the high surrounding temperature more rapidly. This, in turn, causes the thermal runaway
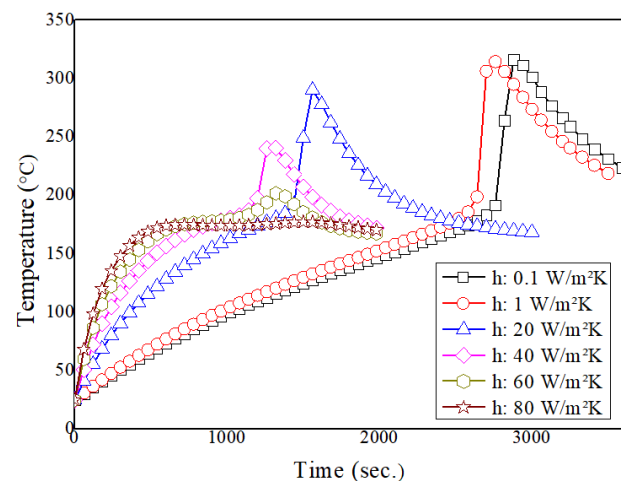

Figure 13 Thermal runaway temperature as a function of the convective heat transfer coefficient at 165 °C.

reactions to start earlier and reduces the triggering time. Furthermore, the increase in the heat transfer coefficient also raises the battery's thermal runaway threshold. It is somewhat counterintuitive that a higher convective heat transfer coefficient—which causes a faster rise in battery temperature and a higher internal temperature gradient—tends to reduce both the probability and intensity of thermal runaway. The reason for this is that, with an increased convective heat
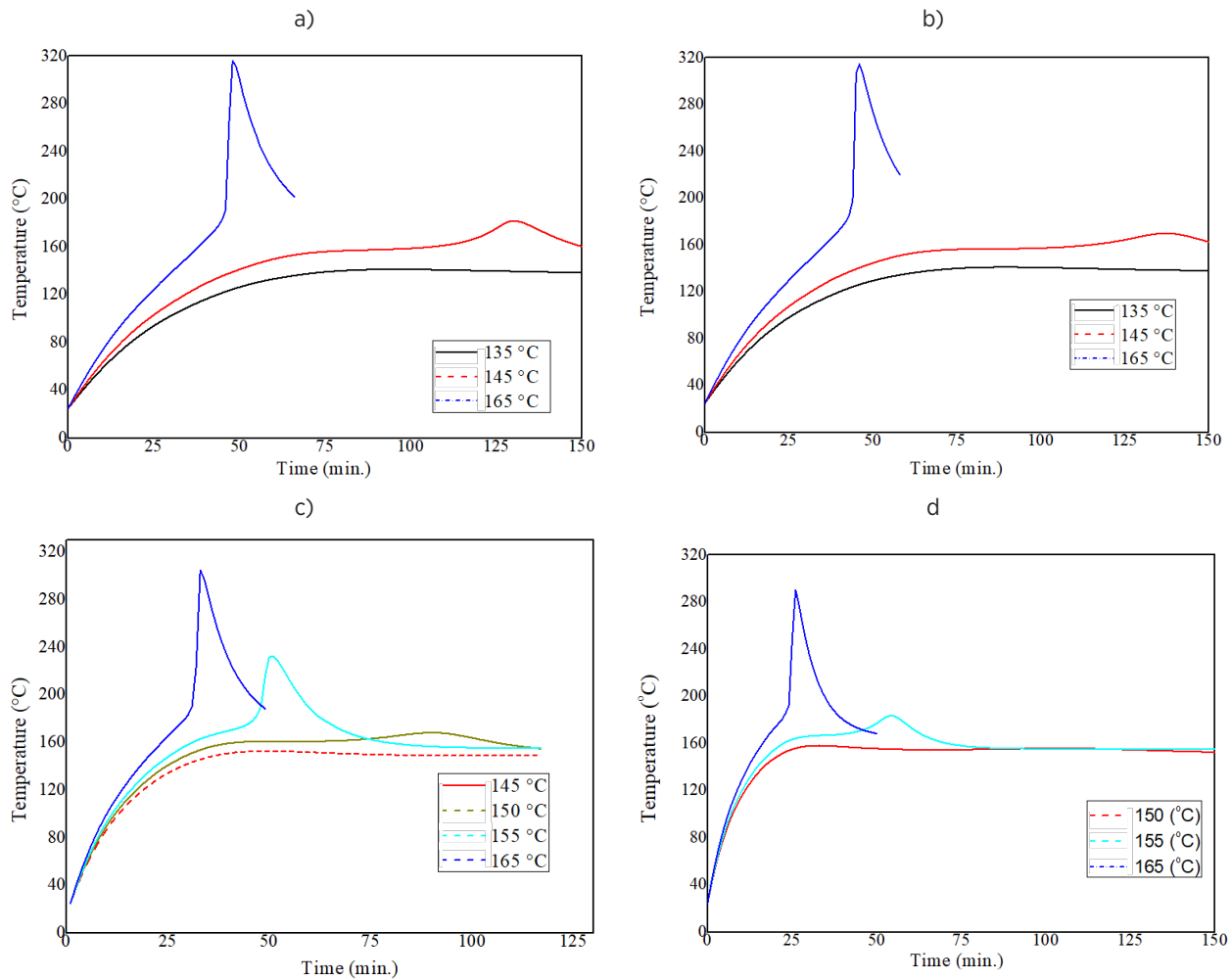
Figure 14 Computed furnace temperature responses for different convective heat transfer coefficients: a) h:0.1 W/m²K, b) h:1 W/m²K, c) h:10 W/m²K, d) h:20 W/m²K.

transfer coefficient, the heat generated by side reactions during the thermal runaway process is more effectively dissipated into the oven environment. A high convective heat transfer coefficient ensures that the heat resulting from solid electrolyte decomposition and side reactions within the electrolyte is transferred to the oven environment before triggering further electrolyte decomposition. At an ambient temperature of 165 °C, thermal runaway occurs aggressively when the convective heat transfer coefficient of the surrounding air is 0.1 W/m²K. However, when the convective heat transfer coefficient is 80 W/m²K, an ambient temperature of 165 °C does not lead to the occurrence of thermal runaway.

In forced air-cooled battery thermal management systems, increasing the airflow rate enhances the removal of waste heat generated by battery cells and reduces the likelihood of thermal runaway propagation. Figure 14 presents the computed furnace temperature responses for different convective heat transfer coefficients. Even under adiabatic conditions, thermal runaway does not occur below 110 °C. At 0.1 W/m²K, a sudden temperature rise is observed above 144 °C. As the convective

heat transfer coefficient increases, the critical temperature for thermal runaway rises: 150 °C at 10 W/m²K and 166 °C at 80 W/m²K. These results highlight the importance of battery thermal management in abuse scenarios. Proper cooling can significantly mitigate thermal runaway risks.

Figure 15 shows the thermal distribution depending on the module cell enclosure material when the 6th cell is forced into thermal runaway with a 20 W heater pad. While the numerical model captures the initiation and progression of thermal runaway, it does not fully reflect maximum temperatures due to unmodeled gas pressure, temperature spikes, and ignition events. Experimental data were therefore used to evaluate propagation. Only the 6th cell was initiated, and other cells were analyzed without runaway formation.

Polyamide composites are widely used in automotive, electronics, and sports applications due to their high impact resistance, thermal stability, and superior mechanical properties [49]. In this study, when the module with polyamide housing was subjected to thermal runaway by heating the 6th cell with a 20 W heater pad, neighbor cells exceeded 90 °C at 980 s and reached 122 °C at 1694 s, below the critical runaway

	500. sn	750.sn	1000. sn	1250. sn	1500. sn	1750. sn	2000. sn
Polyamide							
Aerogel							
Flame-resistant graphite composite							
Epoxy-filled carbon fiber							
Rubber							
Mica							
Polypropylene							
Polystyrene							
PVC							
Ceramic							
Ceramic fiber							
Teflon							

Temperature (C)
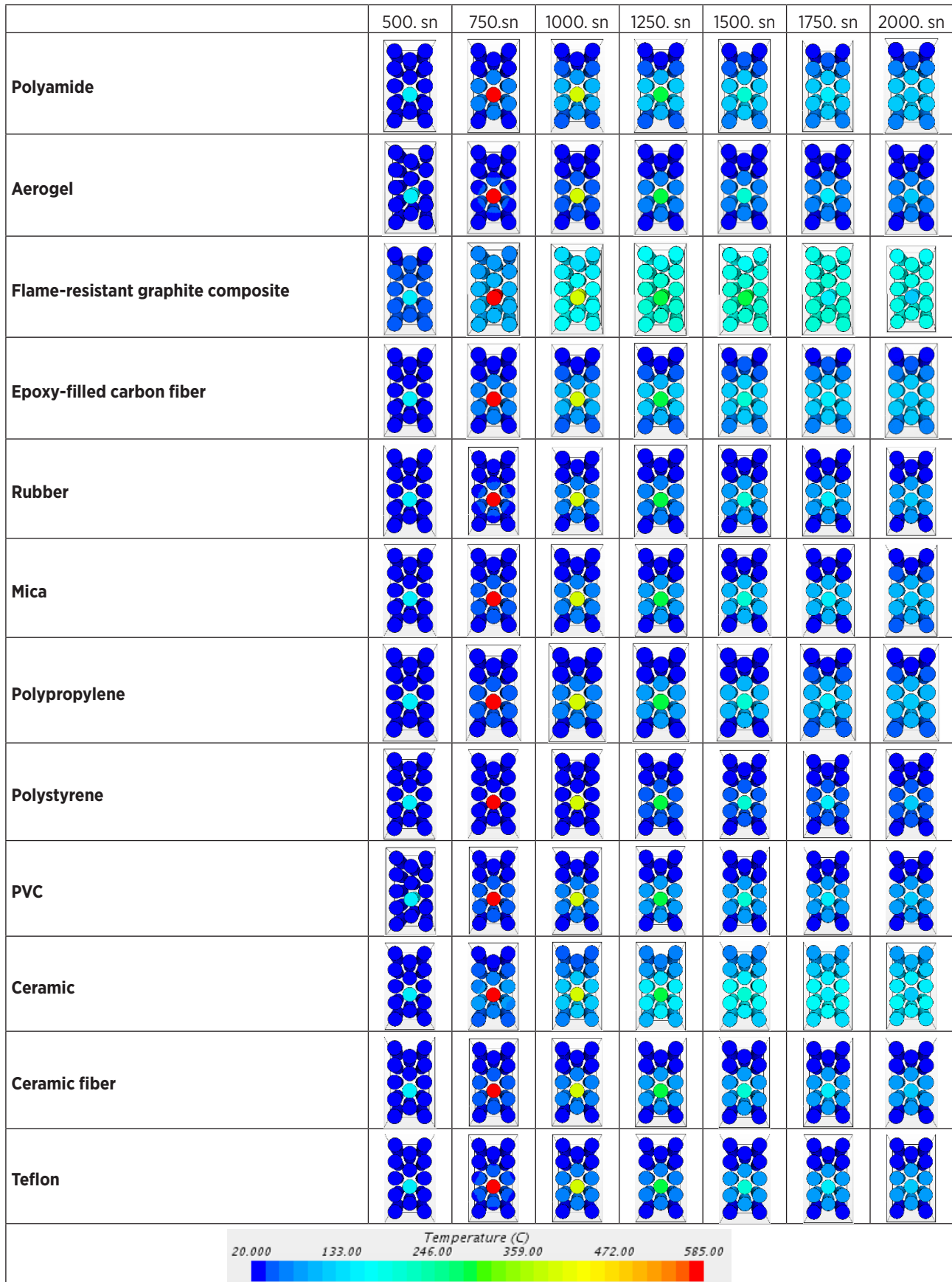20.000   133.00   246.00   359.00   472.00   585.00

Figure 15 Effect of inducing thermal runaway in the 6th module cell with a 20 W heater pad on the module temperature distribution.

threshold. However, the absence of latent heat absorption or high-capacity heat sinking means polyamide acts mainly as a delay mechanism rather than a full suppression medium.

Fiber-reinforced composites are widely used in various fields, including sports equipment, automobiles, and protective clothing, due to their high strength and lightweight properties. These materials, with their low thermal conductivity, support thermal insulation when used under appropriate conditions. Considering the low weight and high strength advantages, they could protect the system from potential battery explosions without significantly increasing system weight [48-50]. With an epoxy-filled carbon fiber enclosure, neighbor cells reached 90 °C at 976 s and 121.7 °C later. Additionally, decomposition of epoxy binders above ~350 °C introduces volatile byproducts that may accelerate ignition, limiting safety without flame-retardant additives.

Graphite composites reached 216.4 °C at 1479 s, the highest temperatures among tested materials. Their superior thermal conductivity, beneficial in aerospace heat dissipation applications, becomes detrimental here by transferring heat directly to adjacent cells without absorption or buffering. This suggests graphite is incompatible with passive-only configurations.

Ceramic materials delayed degradation due to high-temperature endurance; however, heat accumulation raised cell temperatures to 169.2 °C at 1653 s. Dense ceramics offer structural fire resistance but have low volumetric heat capacity, causing heat to store rather than dissipate. Conversely, ceramic fiber structures—which feature micro-porous, low-conductivity pathways—limited neighboring cell temperatures to 79.5 °C, preventing propagation. Their effectiveness stems from combined thermal shock resistance, high porosity, and substantial heat diffusion path length, making them suitable for standalone thermal barriers.

Materials such as rubber, polystyrene, PVC, and Teflon maintained peak temperatures below 90 °C (79.7, 48.97, 85.82, and 85.55 °C). While thermally insulating, their relatively low decomposition or ignition temperatures restrict their application in real battery packs despite good experimental results. Mica and polypropylene allowed temperatures of 96.9 °C and 100.04 °C, initiating TR but remaining below levels associated with explosive ignition, indicating partial mitigation rather than full protection.

Overall, tested enclosures primarily function as thermal delay and structural containment mechanisms, but their lack of latent heat storage or convective cooling means they cannot suppress TR under high heat flux conditions. Their limitations become clear when benchmarked against hybrid strategies in literature.

Compared to these hybrid strategies, the materials tested in this study offer delay rather than suppression, highlighting that passive enclosure materials alone are insufficient for complete TR mitigation. When integrated with PCM or active cooling, materials such as carbon-based structures (for conduction) and ceramic fibers (for insulation) may contribute to multilayer safety architectures, whereas polymers provide mechanical containment but limited heat buffering.

CONCLUSION

In this study, both experimental and numerical analyses were conducted to evaluate the onset and propagation of thermal runaway in lithium-ion batteries. The key findings can be summarized as follows:

1. Critical temperature thresholds: Exothermic reactions initiate above 90 °C, while severe electrolyte decomposition, fire, or explosion occur at 150 °C and beyond.

2. Role of convection: A higher convective heat transfer coefficient significantly delays the onset of TR by dissipating side-reaction heat, thereby improving overall safety.

3. Material influence: Aerogel and ceramic fiber provide superior thermal insulation, while polystyrene offers the most practical compromise between cooling efficiency in normal operation and isolation during TR.

4. Design implications: Effective thermal management must balance two contradictory requirements—high thermal conductivity for cooling and strong inter-cell insulation for safety.

Overall, the results demonstrate that TR mitigation is achievable through careful integration of thermal management strategies and optimized selection of enclosure materials. These insights can guide the design of safer, lighter, and more reliable battery systems for electric vehicles and energy storage applications.

References
1. Lorente DB, Mandil G, Svecova L, Thivel P, Zwolinski P. Life cycle and sustainability. In: Lithium process chemistry: resources, extraction, batteries and recycling. Elsevier; 2015. p. 269–288.
2. Yin Y, Zhang T, Dai Z, Wei T, Qiu X. Experimental and numerical modeling of the heat generation characteristics of lithium iron phosphate battery under nail penetration. Therm Sci. 2024;28(2):1651–1664. doi:10.2298/TSCI230402196Y.
3. Aydın S, Yiğit KS, Savcı İH. Survey of air battery thermal management on the autonomous mobile robots. Therm Sci. 2023;27(5 Pt A):3561–3577. doi:10.2298/TSCI220805022A.
4. United Nations Economic Commission for Europe (UNECE). Regulation No. 100: Uniform provisions concerning the approval of vehicles with regard to specific requirements for the electric power train [2015/505]. Geneva: UNECE; 2015.
5. TÜV SÜD. UN/DOT 38.3 transportation testing – lithium batteries [Internet]. TÜV SÜD; [cited 2025 Sep 30]. Available from: https://www.tuvsud.com/en-us/industries/mobility-and-automotive/automotive-and-oem/automotive-testing-solutions/battery-testing/un-dot-38-3/

6. BBC News. Safety worries lead US airline to ban battery shipments [Internet]. 2015 Mar 3 [cited 2025 Sep 30]. Available from: https://www.bbc.com/news/technology-31709198

7. NBC News. Samsung finally explains the Galaxy Note 7 exploding battery mess [Internet]. 2016 Jan 11 [cited 2025 Sep 30]. Available from: https://www.nbcnews.com/tech/tech-news/samsung-finally-explains-galaxy-note-7-exploding-battery-mess-n710581

8. ETN News. Battery fire risks over the years: concerns & mitigation [Internet]. ETN News; 2021 Dec 27 [cited 2025 Sep 30]. Available from: https://etn.news/e-mobility-blogs/battery-fire-risks-over-the-years-concerns-mitigation

9. Schuler M. Thermal runaway of lithium-ion battery destroys tanker's bridge [Internet]. gCaptain; 2023 Nov 9 [cited 2025 Sep 30]. Available from: https://gcaptain.com/thermal-runaway-of-lithium-ion-battery-destroys-tankers-bridge/

10. Sundén B. Thermal management of batteries. In: Hydrogen, batteries and fuel cells. United States: Academic Press; 2019. p. 93–110. doi:10.1016/C2018-0-01247-5

11. Siddique ARM, Mahmud S, Van Heyst B. A comprehensive review on a passive (phase change materials) and an active (thermoelectric cooler) battery thermal management system and their limitations. J Power Sources. 2018;401:224–237. doi:10.1016/j.jpowsour.2018.08.094

12. Wu S, Lao L, Wu L, Liu L, Lin C, Zhang Q. Effect analysis on integration efficiency and safety performance of a battery thermal management system based on direct contact liquid cooling. Appl Therm Eng. 2021;201:117788. doi:10.1016/j.applthermaleng.2021.117788

13. Jaguemont J, Bardé F. A critical review of lithium-ion battery safety testing and standards. Appl Therm Eng. 2023;231:121014. doi:10.1016/j.applthermaleng.2023.121014

14. Wang Z, Chen S, He X, Wang C, Zhao D. A multi-factor evaluation method for the thermal runaway risk of lithium-ion batteries. J Energy Storage. 2022;45:103767. doi:10.1016/j.est.2021.103767

15. Stering J, Tattersall L, Bamber N, De Cola F, Murphy A, Millen SLJ. Composite structure failure analysis post lithium-ion battery fire. Eng Fail Anal. 2024;160:108163. doi:10.1016/j.engfailanal.2024.108163

16. Jeon CH, Lee Y, Kim R, Kim S, Kim DK. Development of equivalent circuit model for thermal runaway in lithium-ion batteries. J Energy Storage. 2023;74:109318. doi:10.1016/j.est.2023.109318

17. Moghaddam SMH. Designing battery thermal management systems (BTMS) for cylindrical lithium-ion battery modules using CFD [MSc thesis]. Stockholm: KTH School of Industrial Engineering and Management; 2019. Available from: https://kth.diva-portal.org/smash/record.jsf?pid=diva2:1290856

18. Hatchard TD, MacNeil DD, Basu A, Dahn JR. Thermal model of cylindrical and prismatic lithium-ion cells. J Electrochem Soc. 2001;148(7):A755–A761. doi:10.1149/1.1377592

19. Parhizi M, Jain A, Kilaz G, Ostanek JK. Accelerating the numerical solution of thermal runaway in Li-ion batteries. J Power Sources. 2022;538:231531. doi:10.1016/j.jpowsour.2022.231531

20. Ostanek J, Li W, Mukherjee PP, Crompton KR, Hacker C. Simulating onset and evolution of thermal runaway in Li-ion cells using a coupled thermal and venting model. Appl Energy. 2020;268:114972. doi:10.1016/j.apenergy.2020.114972

21. Kim G, Pesaran A, Spotnitz R. A three-dimensional thermal abuse model for lithium-ion cells. J Power Sources. 2007;170(2):476–489. doi:10.1016/j.jpowsour.2007.04.018

22. Peng P, Sun Y, Jiang F. Thermal analyses of LiCoO$_2$ lithium-ion battery during oven tests. Heat Mass Transfer. 2014;50(10):1405–1416. doi:10.1007/s00231-014-1353-x

23. Özdemir T, Ekici Ö, Köksal M. Numerical and experimental investigation of the electrical and thermal behaviors of Li-ion batteries under normal and abuse operating conditions. J Energy Storage. 2024;77:109880. doi:10.1016/j.est.2023.109880

24. Shen M, Gao Q. Structure design and effect analysis on refrigerant cooling enhancement of battery thermal management system for electric vehicles. J Energy Storage. 2020;32:101940. doi:10.1016/j.est.2020.101940

25. Chen W, Hou S, Shi J, Han P, Liu B, Wu B, Lin X. Numerical analysis of novel air-based Li-ion battery thermal management. Batteries. 2022;8(9):128. doi:10.3390/batteries8090128

26. Bugryniec P, Davidson JN, Brown SF. Computational modelling of thermal runaway propagation potential in lithium iron phosphate battery packs. Energy Rep. 2020;6(5):189–197. doi:10.1016/j.egyr.2020.03.024

27. Jaguemont J, Van Mierlo J. A comprehensive review of future thermal management systems for battery-electrified vehicles. J Energy Storage. 2020;31:101551. doi:10.1016/j.est.2020.101551

28. Li A, Yuen ACY, Wang W, Weng J, Lai CS, Kook S, Yeoh GH. Thermal propagation modelling of abnormal heat generation in various battery cell locations. Batteries. 2022;8(11):216. doi:10.3390/batteries8110216

29. Zhong G, Li H, Wang C, Xu K, Wang Q. Experimental analysis of thermal runaway propagation risk within 18650 lithium-ion battery modules. J Electrochem Soc. 2018;165(9):A1925–A1934. doi:10.1149/2.0461809jes

30. Silva GM, Lima TJ, Silva DD, Henriques IB. Assessment of thermal runaway propagation in lithium-ion battery modules with different separator materials. Int J Therm Sci. 2024;197:108836. doi:10.1016/j.ijthermalsci.2024.108836

31. Lee C, Said AO, Stoliarov SI. Passive mitigation of thermal runaway propagation in dense 18650 lithium-ion cell assemblies. J Electrochem Soc. 2020;167:090524. doi:10.1149/1945-7111/ab8978

32. Quan T, Xia Q, Wei X, Zhu Y. Recent development of thermal insulating materials for Li-ion batteries. Energies. 2024;17(17):4412. doi:10.3390/en17174412

33. Li Q, Yang C, Smith K, Keyse M, Pesaran A. Numerical investigation of thermal runaway propagation induced by internal short circuits in Li-ion cells. ECS Meet Abstr. 2017;MA2017-01:288. doi:10.1149/MA2017-01

34. Yuan C, Wang Q, Wang Y, Zhao Y. Inhibition effect of different interstitial materials on thermal runaway propagation in the cylindrical lithium-ion battery module. Appl Therm Eng. 2019;153:39–50. doi:10.1016/j.applthermaleng.2019.02.127

35. Zhao L, Li W, Luo W, Zheng M, Chen M. Numerical study of critical conditions for thermal runaway of lithium-ion battery pack during storage. J Energy Storage. 2024;84:110901. doi:10.1016/j.est.2024.110901

36. Nambisan PHM, Ravadi PR, Reddy HPGM, Kulkarni MA, Sundaram S. Characterization of commercial thermal barrier materials to prevent thermal runaway propagation in large format lithium-ion cells. J Energy Storage. 2023;74:109414. doi:10.1016/j.est.2023.109414

37. Yang T, Xu H, Xie C, Xu L, Liu M, Chen L, Xin Q, Zeng J, Zhang H, Xiao J. A thermal runaway protection strategy for prismatic lithium-ion battery modules based on phase change and thermal decomposition of sodium acetate trihydrate. Batteries. 2025;11:198.

38. Liu X, Zhou Z, Wu WT, Wei L, Wu W, Li Y, Gao L, Li Y, Song Y. Modelling for the mitigation of lithium-ion battery thermal runaway propagation by using phase change material or liquid immersion cooling. Case Stud Therm Eng. 2023;52:103749.

39. Ji W, Dang Y, Yu Y, Zhou X, Li L. Combination of phase change composite material and liquid-cooled plate prevents thermal runaway propagation of high-specific-energy battery. Appl Sci. 2025;15:1274.

40. Aydın S, Samancıoğlu UE, Savcı İH, Yiğit KS, Çetkin E. Impact of cooling strategies and cell housing materials on lithium-ion battery thermal management performance. Energies. 2025;18(6):1379. doi:10.3390/en18061379

41. Zhang S, Sun J, Jia Y, Liu H, Sun G, Li L, Bai D. Low shrinkage and robust polyimide/ultrafine glass fiber aerogel for efficient heat resistance and oil/water separation. ACS Appl Polym Mater. 2025;7(2):622–631. doi:10.1021/acsapm.4c02744

42. Shi W, Wan M, Tang Y, Chen W. Ceramic fiber-reinforced polyimide aerogel composites with improved shape stability against shrinkage. Gels. 2024;10:327. doi:10.3390/gels10050327

43. Li J, Guo P, Hu C, Pang S, Ma J, Zhao R, Tang S, Cheng HM. Fabrication of large aerogel-like carbon/carbon composites with excellent load-bearing capacity and thermal-insulating performance at 1800 °C. ACS Nano. 2022;16(4):6565–6577. doi:10.1021/acsnano.2c00943

44. Liu F, Jiang Y, Peng F, Feng J, Li L, Feng J. Fiber-reinforced alumina–carbon core-shell aerogel composite with heat-induced gradient structure for thermal protection up to 1800 °C. Chem Eng J. 2023;461:141721. doi:10.1016/j.cej.2023.141721

45. Cao Y, Wang K, Wang Z, Wang J, Yang Y, Xu X. Utilization of liquid nitrogen as efficient inhibitor upon thermal runaway of 18650 lithium-ion battery in open space. Renew Energy. 2023;206:1097–1105. doi:10.1016/j.renene.2023.02.117

46. Chen G, Richardson TJ. Thermal instability of olivine-type LiMnPO$_4$ cathodes. J Power Sources. 2010;195(4):1221–1224. doi:10.1016/j.jpowsour.2009.08.046

47. Koluman Plastik. Poliamid 66 [Internet]. Available from: http://www.kolumanplastik.com/tr/urunler/poliamid-66 [cited 2025 Sep 30].

48. Nguyen PL, Vu XH, Ferrier E. Thermo-mechanical performance of carbon fiber reinforced polymer (CFRP), with and without fire protection material, under combined elevated temperature and mechanical loading conditions. Compos Part B Eng. 2019;169:164–173. doi:10.1016/j.compositesb.2019.03.075

49. Kim Y, Ryu K, Na W, Yu J, Lee MW. Origami-inspired reforming method for carbon fiber-reinforced thermoplastics via simple thermal stitching. Compos Part B Eng. 2020;193:108043. doi:10.1016/j.compositesb.2020.108043

50. Kim H, Kim J, Lee J, Lee MWL. Thermal barrier coating for carbon fiber-reinforced composite materials. Compos Part B Eng. 2021;225:109308. doi:10.1016/j.compositesb.2021.109308